Geophysical Research Letters

Supporting Information for

Origin of a preferential avulsion node on lowland river deltas

A. J. Chadwick[1*], M. P. Lamb[1], A.J. Moodie[2], G. Parker[3], J.A. Nittrouer[2]

[1]Division of Geological and Planetary Sciences, California Institute of Technology, 1200 E. California Boulevard, Pasadena, California 91125, USA, [2]Department of Earth, Environmental and Planetary Science, Rice University, Houston, Texas, USA, [3]Department of Civil and Environmental Engineering and Department of Geology, University of Illinois at Urbana-Champaign, Urbana, IL, USA

Contents of this file

Introduction

This document contains supplementary figures (Figures S1-S6), tables (Table S1), and elaborations on model treatment of the river mouth & delta front (Text S1), model workflow (Text S2), flow variability parameters (Text S3), non-dimensionalization (Text S4), results during sedimentation of the trunk channel (Text S5), and sensitivity to other input parameters (Text S6) for the manuscript *Origin of a preferential avulsion node on lowland river deltas.*

Text S1. Treatment of the river mouth and delta front

The river mouth and plume set the downstream end of the backwater zone. Previous models of backwater hydrodynamics have considered a fixed river mouth position, resulting in a constant flow-width profile and fixed backwater zone (Lamb et al., 2012; Chatanantavet et al., 2012; Chatanantavet et al., 2014). This is a good approximation over the timescales of flow events considered by these studies, where the degree of sea-level and land-surface change is small compared to the channel depth. However, the timescales of river avulsion are sufficiently long to drive lobe aggradation and drowning on the order of the channel depth, which could drive significant river mouth advance and retreat respectively, resulting in changes to the flow-width profile.

In this study we develop a new approach to modeling backwater zones that may translate over the timescales of river avulsion. The spatio-temporal evolution of flow width is driven by the emergence and submergence of the land surface. At a given time, the location of the river mouth (x_m) is set by the intersection of the floodplain profile η_f with sea-level ξ_o,

$$x_m = x|_{\eta_f(x) = \xi_o} \quad \text{equation S1}$$

where the floodplain elevation is defined as the sum of the bed elevation and channel depth,

$$\eta_f = \eta_b + H_c \quad \text{equation S2}$$

The flow-width profile is a piecewise function of the channel width, assumed constant and uniform upstream of the river mouth, and a linearly spreading plume downstream

$$B = \begin{cases} B_0 & x < x_m \\ B_0 \dfrac{H_c}{H_{nf}} + B_{flare} \dfrac{H_{nf} - H_c}{H_{nf}} & x \geq x_m \end{cases} \quad \text{equation S3}$$

Where B is the flow width, B_0 is the channel width, B_{flare} is the width of the flare, and $H_{nf} = \xi_o - \eta$ is the no-flow depth. Upstream of the river mouth ($x < x_m$), flow is confined by the channel and the flow width is set by the channel width (B_0). Downstream of the mouth ($x \geq x_m$), the unconfined portion of the flow expands laterally to form the river plume. In this setting, B is the depth-averaged width of a submerged channel and a linearly expanding flare,

$$B_{flare} = B_c + 2 \tan\theta \, (x_m - x) \quad \text{equation S4}$$

where θ is the plume spreading angle, here set to fifteen degrees (Lamb et al., 2012; Chatanantavet et al., 2014). When the river mouth progrades into an empty basin with flat topography, $H_c = 0$ and the flow width in equation S3 reduces to the flare width ($B = B_{flare}$). When the land is drowned, the river mouth retreats and a portion of the flow is confined to the submerged channel. The terms $\frac{H_c}{H_{nf}}$ and $\frac{H_{nf}-H_c}{H_{nf}}$ in equation S3 represent the fraction of the no-flow depth that is of width B_0 and width B_{flare} respectively to yield a depth-averaged width of B. This scheme leads to dynamic backwater profiles that advance with river mouth progradation (i.e., increasing x_m) and back-step during shoreline retreat (i.e., decreasing x_m), and conveniently facilitiates numerical stability in our simulations by producing a gradient in width (dB/dx) that is everywhere differentiable.

At the river mouth lateral flow expansion drives an abrupt deceleration of flow, resulting in a mound of sediment that accumulates and steepens. At sufficiently steep slopes,

fluvial sediment transport gives way to gravity flows and avalanching to form a delta front, or foreset. We model the development of delta fronts in terms of a threshold slope condition following Hotchkiss and Parker (1991). A delta front develops at position x_s if the bed steepens to the threshold slope S_a associated with gravity flows and sediment avalanching.

$$x_s = x|_{S \geq S_a} \qquad \text{equation S5}$$

Once a delta front initiates, the slope of the front is fixed at S_a and deposition drives progradation of the new delta front and delta toe according to shock-capturing conditions (Kostic & Parker, 2003; Parker et al., 2004; Kim et al., 2006; Parker et al., 2008a; Chatanantavet et al., 2014).

Previous work has focused on conditions where the delta front is sufficiently far downstream such that the water velocity is approximately zero. Over longer timescales, however, we find that lobe-switching over antecedent topography can drive the creation of shallow foreset wedges farther upstream, with significant flow velocities at their toes. The foreset wedges pose an order of magnitude discontinuity in bed slope that violates the gradually-varied flow assumption in the backwater equation (Parker, 2004). Across the shallow foreset wedge, we reason the water surface is more accurately described by the Borda-Carnot relationship for flow encountering a sudden expansion (Sturm, 2010).

$$\left(\xi + \frac{U^2}{2g}\right)_u = \left(\xi + \frac{U^2}{2g}\right)_d + \frac{1}{2g}(U_u - U_d)^2 \qquad \text{equation S6}$$

where ξ is the water surface elevation, U is flow velocity, g is acceleration due to gravity, and subscripts u and d denote conditions upstream and downstream of the shallow foreset respectively. We can rearrange to find that this describes a "jump" in the water surface at the lip of the foreset.

$$\frac{\Delta\xi}{H_u} = Fr_u^2(1 - r_A) \qquad \text{equation S7}$$

where $\Delta\xi$ is the increase in water surface elevation from the upstream to downstream end and r_A is the ratio of the upstream to downstream cross-sectional areas of the flow. For the low Froude number scenarios considered in our study, water surface deflections are limited to 1-5% of the flow depth measured upstream of the foreset. Nevertheless, this treatment is important for avoiding erroneous and unstable application of the backwater formula to reaches with a steep, thin delta front. Downstream of the foreset, the flow can again be adequately described in terms of quasi-steady, gradually varied flow.

Text S2. Model workflow

Our simplified modeling scenario consists of an initial planar delta surface with a topset slope equal to the normal flow bankfull transport slope (S_0), a delta foreset slope equal to five times the topset slope ($S_a = 5S_0$) (Borland, 1971; Hotchkiss & Parker, 1991), and a horizontal basin floor. We vary water discharge at the upstream end, and co-vary sediment supply such that all discharges have the same equilibrium transport slope, simulating an alluvial river profile that is always at transport capacity and isolating backwater effects from long-term adjustment in riverbed slope due to changes in sediment-supply and water-discharge ratios (Dade & Friend, 1998; Paola, 2000; Parker et al., 2004; Church, 2006; Ganti et al., 2016b). For each timestep, the river mouth is identified according to S14 and any developing shock fronts

are detected using equation S5. The backwater equation is solved using an upwind predictor-corrector scheme applied to equation 2, except across foreset wedges where equation S7 is locally applied. Next, sediment is routed upstream of the foreset wedge with equation 3 utilizing a "ghost node" at the upstream end (Parker 2004). After routing water and sediment, the delta foreset and riverbed profile η_b for the next timestep are calculated using a finite-difference approximation of equation 1 in a moving-boundary formulation that is explicit, centered in space, and forward in time (Kostic & Parker, 2003; Parker et al., 2004). We update the floodplain elevation profile using equation S2, assuming the channel depth profile is equal to the flow depth profile (equation 2) under bankfull discharge conditions. The updated floodplain profile is used to determine the superelevation using equation 5, and also determines the river mouth for the next timestep via Equation S1. We repeat this numerical scheme, stepping through time until the avulsion threshold is exceeded somewhere along the long-profile according to equation 4. At this point an avulsion occurs, and avulsion length is measured by the stream-wise distance along the parent channel between the avulsion location and the river mouth.

We find that stable numerical simulation requires an especially small timestep when large floods erode the bed near the river mouth and drive progradation of the delta front. For computational expendience, we employ a discharge-dependent CFL condition based on rates of change of bed topography near the river mouth, maintaining numerical stability during high flows and vastly speeding up model simulation during low flow periods where smaller timesteps are not necessary. This is in contrast to previous users of this technique, who have employed a constant river discharge (Kostic & Parker, 2003) or abandoned the moving-boundary framework during high flow events (Chatanantavet et al. 2012). Because the floodplain profile is set by the bankfull-water-surface profile (equation S15), changes in the bankfull flow depth over time violate equation 1. However, we note found that changes in the bankfull flow depth over time were so small that the error in mass-balance incurred is acceptable – it is less than the ~3% truncation error introduced by our numerical scheme, which is a common value for similar morphodynamic models (Parker, 2004) – and should not significantly affected modeled avulsions.

In our simulations we have imposed four delta lobes, represented by four one-dimensional stream-wise long profiles in parallel. At a given time, a single lobe is actively routing flow, and the other three lobes are abandoned. When the active lobe experiences avulsion, flow finds a new path downstream of the avulsion location along one of the abandoned lobes, and the flow path upstream remains unchanged,

$$\eta_{b,new}(x) = \begin{cases} \mathrm{MIN}\left(\eta_{b,abandoned1}(x), \eta_{b,abandoned2}(x), \eta_{b,abandoned3}(x)\right) & x > x_A \\ \eta_b(x) & x \le x_A \end{cases} \quad \text{eq. S8}$$

where x is distance downstream, x_A is the avulsion location, $\eta_{b,new}$ is the new riverbed profile after avulsion, η_b is the riverbed profile before avulsion, and $\eta_{b,abandoned1}$, $\eta_{b,abandoned2}$, and $\eta_{b,abandoned3}$ are the three abandoned lobe long profiles. The MIN operator here selects the abandoned profile that has the minimum mean elevation, $\bar{\eta}_b$, downstream of the avulsion node,

$$\bar{\eta}_b = \frac{1}{x_m - x_A}\int_{x_A}^{x_m} \eta_b(x)\, dx \qquad \text{equation S9}$$

where x_m is the downstream coordinate of the river mouth. For example, if $\eta_{b,abandoned2}(x)$ yields a lower value of $\bar{\eta}_b$ than both $\eta_{b,abandoned1}(x)$ and $\eta_{b,abandoned3}(x)$ yield, then $\eta_{b,abandoned2}(x)$ is selected as the path downstream of the avulsion location. This simple selection scheme mirrors the tendency of river deltas to fill in topographic lows when avulsing (Straub et al., 2009).

Text S3. Flow variability parameters

In this study, we explore how deltaic avulsion patterns respond to upstream flow regimes and downstream changes in relative-sea-level through the systematic variation of these variables on a base case of the model that is characteristic of large, low-sloping deltas. Flow variability is parameterized in terms of a distribution of flow events with varying frequency, magnitude, and duration. Table S1 provides field examples of the relevant parameters, and summarizes the range of parameter space explored in this study.

The water discharge of alluvial rivers can fluctuate across a range of timescales, but generally stage height will fill the channel banks on a recurrence interval of ~2 years (Wolman & Miller, 1960). Many have argued that the morphodynamics of alluvial rivers can be well-approximated using an intermittency factor and a constant discharge that is equal to this bankfull condition, on the grounds that the bankfull flood represents a balance of frequency and magnitude that has the maximum impact on alluvial form (Wolman & Miller, 1960; Andrews, 1980; Parker et al., 2007). However, this approximation should break down for rivers in their backwater zone, where the downstream boundary enhances deposition during lower-than-bankfull flows and drives erosion during larger floods (Lamb et al., 2012). We explicitly model variable flows using a log-normal distribution of stage height upstream in the normal-flow reach. A log-normal distribution of stage height sufficiently describes flow in many river systems measured on a monthly-mean basis (Stedinger et al., 1993; Leboutillier & Waylen, 1993; Lague et al., 2005), and is uniquely defined by a bankfull-exceedence probability and a coefficient of variation (Figure S1). The bankfull exceedence probability F_{bf} describes the frequency of overbank flows relative to all possible flows, and can range from zero to unity. On many low-gradient alluvial rivers, monthly-averaged flows will exceed bankfull between 1-10% of the time, corresponding roughly to a 1-2 year recurrence flood (Langbein & Leopold, 1964). The coefficient of variation (CV) describes the magnitude of low flows and high flows relative to the average flow, and is defined by the standard deviation of the stage height divided by the mean. Among the lowland deltas considered in table S1, the coefficient of variation ranges from 0.18-0.91.

In our numerical model, we discretize the distribution into twenty logarithmically spaced bins that span from low flow (less than bankfull) to high flow (greater than bankfull) conditions. Over time, each bin is randomly sampled at a defined event timescale, $\boldsymbol{T_e}$. In our scaled framework the normalized event timescale ($\boldsymbol{T_e^* = T_e/T_{adj}}$) describes how long flow events persist relative to channel adjustment timescale, the time required for those flows to transport enough sediment to aggrade the backwater reach by one channel depth. Based on previous work (Chatanantavet et al. 2014), we expect flow regimes to maintain bed disequilibrium and a persistent backwater zone when the normalized event timescale is much less than unity. This condition is satisfied for many deltaic rivers, where we calculate $\boldsymbol{T_e^* = 10^{-4} - 10^{-1}}$. If $\boldsymbol{T_e^* > 1}$,

individual flow events may persist long enough to mute backwater effects through aggradation or degradation of the river profile to quasi-uniform flow conditions.

Text S4. Non-dimensionalization

Our simulations explore how deltaic avulsion patterns respond to river flow regime, relative sea-level rise, and initial topography by systematically varying the discharge and sea-level parameters. We non-dimensionalize the model to develop a framework that can be applied to a wide range of river conditions, reduce the number of model inputs, and identify key controls on model behavior. Channel-bed elevation ($\boldsymbol{\eta_b}$) is scaled in terms of bankfull channel depth in the normal-flow reach, flow width ($\boldsymbol{B}$) is scaled in terms of the channel width in the normal-flow reach, and stream-wise distance ($\boldsymbol{x}$) is scaled in terms of the backwater length-scale,

$$\eta_b = \eta_b^* H_0 \qquad \text{equation S10}$$

$$B = B^* B_0 \qquad \text{equation S11}$$

$$x = x^* L_b = x^* \left(\frac{H_0}{S_0}\right) \qquad \text{equation S12}$$

where $\eta^*$is dimensionless channel-bed elevation, $B^*$is dimensionless flow width, x^* is dimensionless distance downstream, and H_0, B_0, and S_0 are the channel depth, width, and slope in the normal-flow reach upstream. We also scale time (t) in terms of the time required to fill a backwater reach with the sediment supply. Here, we modify the bed-adjustment timescale to apply to a sinuous channel that exchanges sediment with its nearby floodplain, making the simplifying assumption that floodplain width (B_f), channel sinuosity (Ω), deposit porosity (λ_p), and the ratio of wash load to bed-material load (Λ) are constant and uniform,

$$t = t^* T_0 = \frac{t^* H_0 B_f L_b}{\Omega \overline{q_t}} \frac{(1-\lambda_p)}{(1+\Lambda)} \qquad \text{equation S13}$$

where t^* is dimensionless time, T_0 is the reach-filling timescale, and $\overline{q_t}$ is the time-averaged sediment supply per unit width. It should be noted that previous authors have hypothesized that backwater effects may drive downstream fining trends (Nittrouer et al., 2011; Nittrouer et al., 2012; Venditti & Church, 2014; Maselli et al., 2018) and downstream reductions in floodplain and channel-belt width (Fernandes et al., 2016) in some systems, which could alter the bed-adjustment timescale. For example, narrow floodplains will aggrade faster than wide floodplains for the same amount of sediment-flux convergence (Equation 1), and therefore backwater reaches with narrow floodplains adjust more quickly after flood events and may avulse more frequently compared to wider floodplains upstream.

We non-dimensionalize equations 1-3 in the main text by inserting equations S10-S13 and simplifying,

$$\frac{\partial \eta^*}{\partial t^*} + \sigma^* = -\frac{1}{\overline{q}^*_t} \frac{\partial B^* q_t^*}{\partial x^*} \qquad \text{equation S14}$$

$$\frac{\partial H^*}{\partial x^*} = \frac{S^* - S_f^*}{1 - Fr^2} + \frac{Fr^2}{1 - Fr^2} \frac{H^*}{B^*} \frac{dB^*}{dx^*} \qquad \text{equation S15}$$

$$C_f q_t^* = \alpha(\tau^*)^n \qquad \text{equation S16}$$

where $H^* = H/H_0$ is the dimensionless flow depth, $S^* = S/(H_0/L_b)$ is the normalized bed slope, $S_f^* = Fr^2 C_f/S_0$ is the normalized friction slope, q_t^* is the Einstein number representing dimensionless bed-material transport (Einstein, 1950; Parker, 1979) and $\bar{q}^*{}_t$ is the time-averaged Einstein number. We note that η^* in equation S14 is defined as elevation relative to sea level, not relative to the basin floor (as it is defined in some previous work, e.g. Baumanis & Kim, 2018). We prefer this reference frame because it condenses relative sea-level rise into the single parameter σ^*, illustrating that sea-level rise and subsidence have the same effect on sediment mass-balance. While Fr and τ^* are commonly defined in terms of gravity (g) and grain-size (D), we can reduce the number of model inputs by casting them in terms of their counterparts in the normal-flow reach upstream during bankfull conditions.

$$Fr^2 = \frac{U^2}{gH} = Fr_{bf}^2 \frac{C_{f,bf}}{C_f}\left(\frac{1}{B^*}\right)^2\left(\frac{1}{H^*}\right)^3 \qquad \text{equation S17}$$

$$\tau^* = \frac{C_f U^2}{RgD} = \tau_{bf}^* H^* \frac{C_f}{C_{f,bf}}\left(\frac{Fr}{Fr_{bf}}\right)^2 \qquad \text{equation S18}$$

where the subscript bf denotes bankfull conditions in the normal-flow reach. Another important parameter is the dimensionless relative sea-level rise (or basin subsidence) rate,

$$\sigma^* = \frac{\sigma L_b}{\bar{q}_t}\frac{B_f}{\Omega B}\frac{(1-\lambda_p)}{(1+\Lambda)}\,. \qquad \text{equation S19}$$

where σ^* describes the balance of accommodation space created by relative sea-level rise over the active floodplain, as compared to the sediment supply to the backwater reach. When $\sigma^* \ll 1$, sediment supply far outpaces the rate of sea-level rise and we expect lobe growth and avulsion similar to steady sea-level scenarios. As σ^* approaches unity, we expect that sea level will cause intermittent or permanent drowning of delta lobes and potentially affect the location of avulsions. This parameterization is similar to the "A/S" ratio concept" of Muto and Steel (1997, 2002) and similar theories for radially averaged deltas (Galloway, 1989; Paola et al., 2011; Liang et al., 2016) but is here applied to avulsion cycles and discrete deltaic lobes.

Inserting equation S10 into equation 4, we find the equation for normalized avulsion setup,

$$\Delta\eta^* \geq H^* H_c^* \qquad \text{equation S20}$$

where $\Delta\eta^* = \Delta\eta/H_0$ is normalized superelevation and $H_c^* = H_c/H_0$ is the dimensionless channel depth. The avulsion threshold H^* is equal to fifty percent of the channel depth $(H^* = 0.5)$ for all our simulations presented here, representing a value that is consistent with field and laboratory observations (Mohrig et al., 2000; Ganti et al., 2016b). However, field evidence suggests that the avulsion threshold is systematically reduced under flashier discharge regimes in the range of H* = 0.2-1 (Ganti et al., 2014). At each model timestep, normalized superelevation $\Delta\eta^*$ is calculated by inserting equation S10 into equation 5,

$$\Delta\eta^*(x) = \begin{cases} \eta_f^*(x) - \eta_{f,abandoned}^*(x) & \text{for } x^* \leq x_{m,abandoned}^* \\ \eta_f^*(x) - \xi_{sea}^* & \text{for } x^* > x_{m,abandoned}^* \end{cases} \qquad \text{equation S21}$$

where $\eta_f^* = \eta_f/H_0$ is dimensionless floodplain elevation, $x_m^* = x_m/L_b$ is dimensionless river mouth location, $\xi_{sea}^* = \xi_{sea}/H_0$ is dimensionless sea-level elevation, and subscript "abandoned" indicates quantities on the abandoned delta lobe with lowest elevation. The dimensionless avulsion length (L_A^*) is the ratio of the avulsion length (L_A) to the backwater length-scale (L_b),

$$L_A^* = \frac{L_A}{L_b} = \frac{L_A}{H_0/S_0}. \qquad \text{equation S22}$$

For lowland deltas with a preferential avulsion length set by the backwater length, we expect that $L_A^* \sim 1$. We ran our simulations for a total of 13 avulsion cycles, which we found sufficient to capture trends in avulsion location between our different model runs. Running the model for many more avulsion cycles yields similar results but is computationally expensive given the broad parameter space considered in our study.

Text S5. Results for trunk-filling avulsion cycles

Most simulated avulsion cycles feature focused deposition within one backwater length-scale of the river mouth (Figure 2b-c, e-f). However, we also observed occasional avulsion cycles with significant deposition farther upstream in the trunk channel. These trunk-filling avulsion cycles occur when the initial floodplain profile η_f is significantly lower than all other inactive lobes, for example during avulsion cycle 4 (Figure S2). Consequently, the active lobe begins construction with substantially lower superelevation compared to other avulsion cycles, requiring greater aggradation along the entire river long-profile before reaching the avulsion threshold.

Trunk-filling avulsion cycles occurred periodically in all our simulations, usually during cycle number 4, 7, 10, and 13. In simulations with a preferential avulsion node, we observed that trunk-filling avulsion cycles were also associated with downstream translation of the avulsion node (Figure S2b). The avulsion node translated downstream with major shoreline progradation, as a result of greater aggradation of the river long-profile with a constant transport slope. Similar behavior involving a periodic shift in the avulsion node has been documented for the Yellow River in China (Ganti et al., 2014).

During avulsion cycles 8 and 11 in the variable-discharge case, avulsions occurred far upstream of the backwater zone, but without a prominent peak in superelevation. These avulsions were similar to those in the constant-discharge case and were due to a transient period of nearly uniform deposition rate as the trunk channel adjusted to a new profile immediately following trunk-filling avulsion cycles. Occasional avulsions far upstream of a backwater-mediated node have been interpreted from Mississippi River deposits (Chamberlain et al., 2018).

Text S6. Model sensitivity to other parameters

In the main text, we present three conditions that can produce a backwater-scaled avulsion node in our model: 1) a uniformly downstream-sloping initial condition, 2) flow

variability, and 3) rapid sea-level rise. During the course of our analyses, we also explored how, and to what extent, changing other model parameters impacts our main results. Here we discuss the avulsion threshold parameter H^* and the number of imposed delta lobes N which, after the important roles of flow variability, the initial condition, and sea-level rise, we found to have a notable effect on model behavior.

In previous simulations the avulsion threshold was set to $H^* = 0.5$. To relax this assumption, we varied the avulsion threshold across a range comparable to modern deltas ($0.2 \leq H^* \leq 1$, Ganti et al., 2014) under constant-discharge conditions and under variable-discharge conditions, with all other parameters set to the base case (Figure S6). Similar to the scenario of $H^* = 0.5$, a preferential avulsion node emerges only in simulations with flow variability. When avulsions occurred in constant-discharge simulations, a reach of ~2 backwater lengths was within 10% of the avulsion threshold, indicating no dominant avulsion location regardless of the value of H^*. In both constant- and variable-discharge scenarios, increasing the avulsion threshold leads to an increase in the observed avulsion lengths. This is because, at higher values of H^*, lobes prograde farther seaward of the inactive-lobe shoreline, where avulsions are unlikely to occur. Thus, the avulsion threshold influences the location of the avulsion node in our model, but it does not control the occurrence of a preferential avulsion node itself, which still depends on flow variability, initial conditions, or sea-level rise.

The avulsion threshold was set to a constant value during all simulations for simplicity. However, avulsion threshold may not be a constant in reality and may in fact depend on flow variability at different sites, as argued by Ganti et al. (2014). Nonetheless, the sensitivity analysis shows that changing the threshold does not change our main conclusion that flow variability is necessary for emergence of a persistent node. Varying H^* under variable-discharge conditions only shifted avulsion lengths between $0.5L_b$ to $2L_b$ (Figure S5b), which was minor compared to spread in avulsion lengths resulting from a constant discharge (Figure S5a), and also within the scatter of backwater-mediated avulsion lengths observed in the field (Figure 1a).

In previous simulations, we also imposed a fixed number of 4 delta lobes. This was an arbitrary but reasonable choice based on field observations (Pang & Si, 1979; Roberts, 1997; Coleman et al., 1998; Chu et al., 2006) and flume experiments (Reitz et al., 2010; Carlson et al., 2018). We found that changing the number of delta lobes alters the timing of an avulsion node's behavior, but does not affect the occurrence of the avulsion node. For example, the shift from preferential to non-preferential avulsions in the constant-discharge scenario occurs after 4 avulsion cycles in our model (Figure 2A) because we impose four delta lobes, and so it takes 4 avulsions for the delta to bury its initial conditions. On a delta with N discrete lobes, this same behavior occurs after burying the initial conditions, but it requires N avulsion cycles. Other examples include outlier avulsions far upstream of the backwater zone, and downstream translation of the avulsion node, both of which occur every $N - 1$ avulsion cycles in our simulations. Both outlier avulsions and translation of the avulsion node are a consequence of trunk-filling avulsion cycles in our model (Text S5), which occur when all lateral space has been filled and the new lobe is forced to prograde farther seaward than previous lobes, corresponding to every $N - 1$ avulsion cycles after the delta has buried its initial conditions. Thus, simulated deltas with 4 lobes filled their trunk channels every 3 avulsion cycles (usually cycles 4, 7, 10, and 13) and experienced a shift in the avulsion node and then an outlier avulsion. A delta with fewer lobes has less lateral space to fill before advancing seaward, and therefore experiences more frequent filling of its trunk channel, a more mobile avulsion node, and more common outlying avulsion sites.

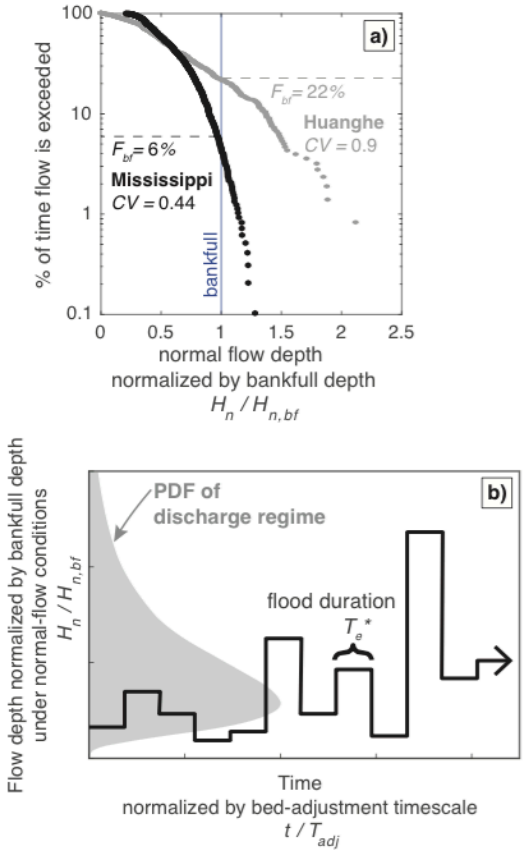

Figure S1. a) Exceedence probability of normal-flow depth normalized by bankfull depth for the Mississippi and Huanghe (Ganti et al., 2014), illustrating how bankfull exceedence probability (F_{bf}) and the coefficient of variation (CV) were estimated in Table 1. Steeper trends of exceedence probability correspond to lower values of CV. b) Schematic time-series of modelled normal-flow depth in after non-dimensionalization, showing how input flow depth is determined by randomly sampling a log-normal distribution for fixed flow events of duration T_e^*.

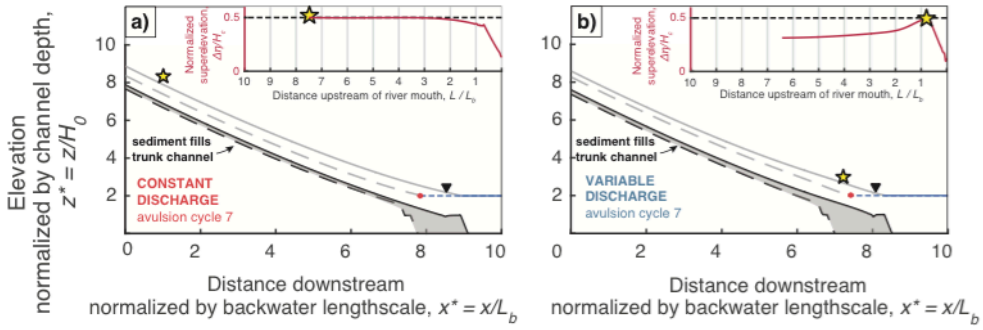

Figure S2. Long profile evolution of avulsion cycle 7 under constant discharge (a) and variable flows (b). Avulsion cycle 7 is an example of a major avulsion cycle where sediment fills the trunk channel and, under variable flows, the avulsion node migrates downstream with shoreline progradation. Black lines are the riverbed profile at the start (dashed) and end (solid) of an avulsion cycle, the floodplain profiles of the active lobe (gray solid line) and the lowest inactive lobe (gray dashed line) are used to calculate superelevation (see insert). Downstream of the inactive-lobe shoreline location (red circle), levee superelevation is measured relative to

sea level. Black triangles are the river mouth at the end of the avulsion cycle. Yellow stars show the avulsion location.

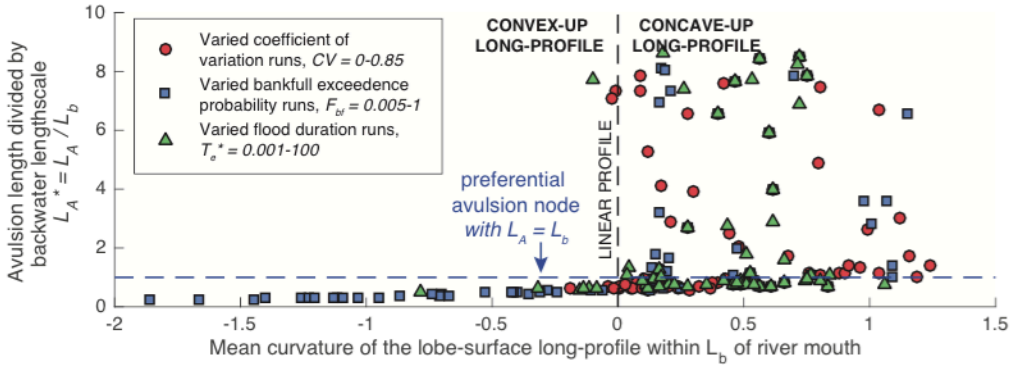

Figure S3. Normalized avulsion length as a function of mean lobe-surface curvature for all simulated avulsion cycles, showing that there is a preferential avulsion node when flow regimes are sufficiently variable to produce a convex-up long profile in the backwater zone. The mean curvature of lobe-surface long profiles (i.e., the x-axis) was calculated by taking the

mean of the second spatial derivative of bed elevation within one backwater length-scale of the river mouth $\left(i.e., \frac{1}{L_b}\int_{x_m-L_b}^{x_m}\frac{\partial^2\eta}{\partial x^2}dx\right)$ using centered finite differences.

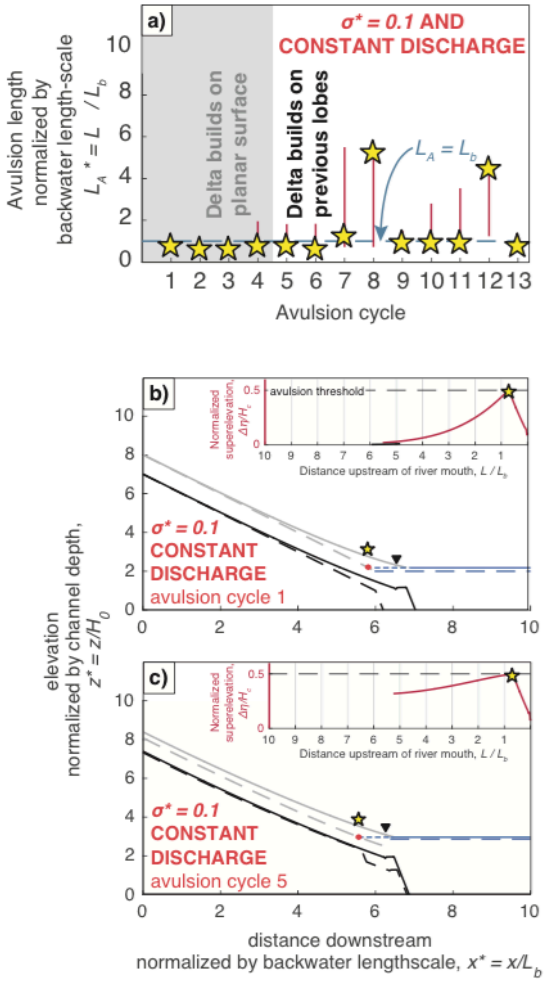

Figure S4. Avulsion length through time (a) and long-profile results (b-c) for constant-discharge conditions and a rapid relative-sea-level-rise rate ($\sigma^* = 0.1$). Rapid relative sea-level rise induces a persistent downstream increase in deposition rate, leading to avulsions near the inactive-lobe shoreline in the absence of backwater effects. Downstream of the inactive-lobe shoreline location (red circle), floodplain superelevation is measured relative to sea level and so the superelevation is reduced despite high aggradation rates. In a), red error bars indicate the portion of the reach within 10% of the threshold superelevation necessary for avulsion. In b-c), black lines are the riverbed profile at the start (dashed) and end (solid) of an avulsion cycle. The floodplain profiles of the active lobe (gray solid line) and the lowest inactive lobe

(gray dashed line) are used to calculate superelevation (see insert). Black triangles are the river mouth at the end of the avulsion cycle. Yellow stars show the avulsion location.

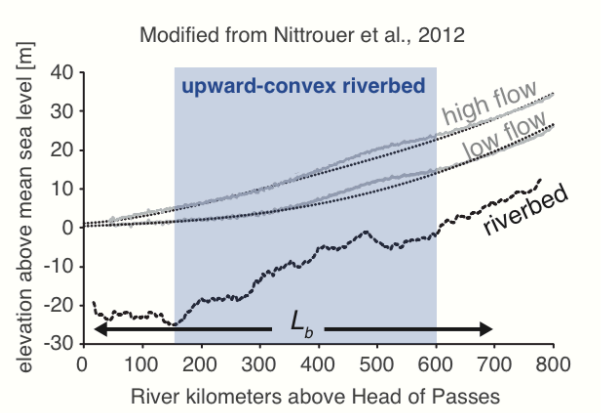

Figure S5. Elevation long profile of the lower Mississippi River's backwater zone, modified from Nittrouer et al., (2012). The riverbed is shown in a black dashed line, and water surfaces during a low flow discharge (7500 m^3/sec) and a high flow discharge (40,000 m^3/sec) are shown based on stage measurements (black dotted lines) and based on a backwater hydrodynamic model (gray lines). The blue shaded region highlights the reach of broad upward-convexity in the riverbed that bears resemblance to riverbed curvature in our

variable-discharge simulations, which in our model resulted from transient riverbed adjustment and co-occurred with a backwater-mediated avulsion node.

Figure S5

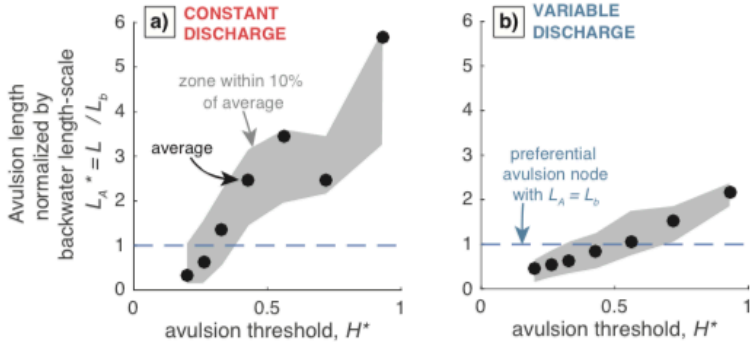

Figure S6. Model results for avulsion length with changing avulsion threshold H^* under constant discharge (a) and variable discharge (b). Each black circle shows the avulsion locations averaged over cycles not influenced by the initial conditions (cycles 5-13), and the

gray shaded areas denote the average reach within 10% of the avulsion threshold at times of avulsion. For all model runs, $Fr_{n,bf} = 0.17,\ \tau^*_{n,bf} = 1,\ C_f = 0.005,$ and $H^*_b = 2$.

		FLOW VARIABILITY PARAMETERS			BASIN PARAMETERS		NORMAL FLOW PARAMETERS AT BANKFULL		
		F_{bf} [-]	CV [-]	T_e^* [-]	σ^* [-]	H_b^* [-]	C_f [-]	$Fr_{n,bf}$ [-]	$\tau_{n,bf}^*$ [-]
NUMERICAL MODEL RUNS	Constant-discharge model run	1	0	N/A	0.0E+00	2.0	0.005	0.17	1.00
	Variable-discharge model run (base case)	0.05	0.53	1.0E-03	0.0E+00	2.0	0.005	0.17	1.00
	Flood-frequency model runs	0.005 - 1	0.53	1.0E-03	0.0E+00	2.0	0.005	0.17	1.00
	Flood-magnitude model runs	0.05	0 - 0.85	1.0E-03	0.0E+00	2.0	0.005	0.17	1.00
	Flow-duration model runs	0.05	0.53	1.0E-03 - 1.0E02	0.0E+00	2.0	0.005	0.17	1.00
	Relative-sea-level-rise model runs	0.05	0.53	1.0E-03	1.0E-03 - 1.0E01	2.0	0.005	0.17	1.00
NATURAL DELTAS	Ganges-Brahmaputra, Bangladesh	0.08	0.68	3.73E-03	7.14E-02	11.4	0.005	0.22	0.88
	Danube River, Romania	0.10	0.27	2.95E-03	7.85E-02	11.1	0.005	0.16	0.66
	Yellow River, China	0.22	0.91	3.77E-01	9.11E-03	8.6	0.005	0.22	2.19
	Mississippi River, USA	0.06	0.44	1.80E-03	1.70E-01	3.8	0.005	0.15	1.88
	Orinoco River, Venezuela	0.43	0.61	7.37E-04	6.08E-02	13.8	0.005	0.17	1.00
	Nile River, Egypt	0.05	0.65	6.39E-02	2.46E-02	7.4	0.005	0.18	1.62
	Parana River, Argentina	0.12	0.18	1.87E-04	1.70E-01	3.4	0.005	0.14	0.98

Table S1. Flow variability parameters, basin parameters and bankfull flow parameters in numerically simulated and natural deltas. F_{bf} is bankfull exceedence probability, CV is the coefficient of variation of normal-flow depth upstream, T_e^* is the dimensionless flow event duration, σ^* is the dimensionless relative-sea-level-rise parameter, H_b^* is dimensionless basin depth, C_f is the friction coefficient, $Fr_{n,bf}$ is the bankfull Froude number in the normal-flow reach, and $\tau^*_{n,bf}$ is the bankfull Shields number in the normal-flow reach. For natural deltas, parameters were calculated using bankfull characteristics reported in Jerolmack and Mohrig (2007) and Chatanantavet et al. (2012), discharge time-series from Ganti et al. (2014), relative-

sea-level-rise rates reported in Syvitski et al., (2009), basin depths reported in Syvitski and Saito (2007), and sediment supplies reported in Milliman and Syvitski (1992).